

Paper draft v1.2 for supersat project

K. Latimer

Jan 7, 2020

Questions/comments from DR in blue

Responses from KL in red

1 Intro

In a recent paper, Fan et al introduce a novel “warm phase invigoration mechanism” (WPIM) in which increased concentrations of ultrafine aerosol particles ($UAP_{<50}$, with 50 signifying an upper bound on particle diameter of 50nm) in the boundary layer (BL) result in enhanced convective updraft speeds and precipitation rates [1]. As pointed out by Grabowski and Morrison, the precise explanation for this physical effect is that, in allowing for lower equilibrium water vapor supersaturation (SS) values in rising convective parcels, these excess aerosol particles lead to an increase in the buoyancy of the parcel over the course of its ascent, thus enhancing convective speeds [2].

In order to get a quantitative intuition for how this works, we offer a simplified version of the calculation in [3], which still conveys the same essential idea. We consider a polluted (non-supersaturated; i.e. $RH = 1$) storm ascending in an environment whose temperature profile has been set by clean storms. The parcel condenses water vapor as it rises, and for simplicity we assume no latent heat is lost to the environment. We then have (see Table 1 for explanation of constants and variables used in the text. We use δ here to represent a variation in state variables between two parcels, as distinguished from d in Equation 5 which denotes a proper differential form):

$$C_{ap}\delta T + L_v\delta q_v = 0, \quad (1)$$

where q_v is the water vapor mass fraction of the parcel ($q_v = m_v/m_{tot}$), also expressed in terms of the relative humidity (RH) and saturation water vapor mass fraction (q_v^*) as:

$$q_v = RHq_v^* \quad (2)$$

Use the Clausius-Clayperon equation:

$$\begin{aligned}
\delta q_v^* &= \delta \left(\frac{e_s V}{R_v T m_{tot}} \right) \\
&= \frac{\delta e_s}{e_s} q_v^* - \frac{\delta T}{T} q_v^* \\
&= \frac{L_v \delta T}{R_v T^2} q_v^* - \frac{\delta T}{T} q_v^* \\
&= \left(\frac{L_v}{R_v T} - 1 \right) \frac{\delta T}{T} q_v^* \\
&\approx \frac{q_v^* L_v}{R_v T^2} \delta T
\end{aligned} \tag{3}$$

Taking the differential of Equation 2 and rearranging terms in Equations 1, 2, and 3 yields:

$$\delta T = \frac{-L_v q_v^*}{C_{pa} + q_v \frac{L_v^2}{R_v T^2}} \delta RH \tag{4}$$

Plugging in typical values for RH (≈ 1.1) and T (≈ 300 K) gives $dT \approx 1$ K.

In their paper (see for example Figure 2(b) of that work), Fan et al provide anecdotal evidence that the WPIM is capable of producing enhancements in vertical wind velocity on the order of 10 m/s for polluted relative to unpolluted storms. Even neglecting diffusive, frictional, or radiative losses, this requires a variation in convective available potential energy ($CAPE$) of ≈ 100 J/kg, or a RH difference between the dirty storm and clean environment of ≈ 0.1 , i.e., the environment must support SS on the order of 10% throughout the troposphere.

While Fan et al do not offer any proof based on experimental data that such high SS exist in the convection setting the environmental lapse rate, they do observe comparable values in numerical simulations. In particular, using the Weather Research and Forecasting (WRF) model to simulate pristine (no $UAP_{<50}$) conditions in the Amazon Rainforest, they find (horizontally- and time-averaged) SS in convective cores of up to 15%.

Since this is well above what is typically reported or assumed in the literature [4, 5, 6, 7, 8, 9, 10, 11, 12], we seek in this paper to determine if we can find experimental evidence for $O(10\%)$ SS in nature. We use data from the High-Altitude Long-range research aircraft (HALO) (part of the ACRIDICON-CHUVA mission in and around Manaus, Brazil in 2014-15), as well as from the first phase of the Cloud Aerosol Interaction and Precipitation Enhancement Experiment (CAIPEEX) in India (taken in June [around Hyderabad] and August [around Bareilly] 2009) [?, 13] as a dataset of opportunity.

2 Data Analysis and Results

[You would want to show the $R2$ (contour map or heat map) as a function of w and LWC thresholds to make this claim. Or, simply say that you tried

many combinations and found this pair of thresholds to be adequate by some subjective criteria.] In order to determine experimental supersaturation within a reasonable margin of error, we must use the quasi-steady-state supersaturation (SS_{QSS}) formula [14]. In order to determine the region of validity for this approximation, we used data from the WRF output, since this allows us to compare to the true supersaturation (here called SS_{WRF}). We focused on the following considerations:

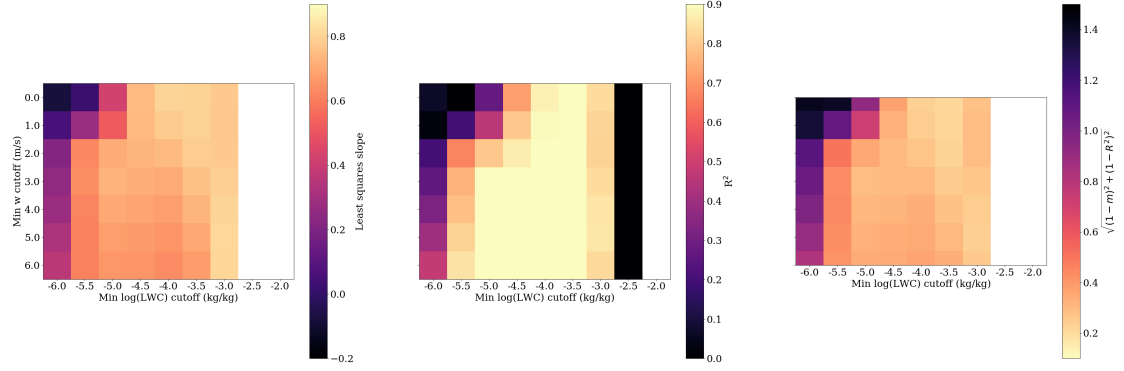
- The QSS approximation should be a good and reliable estimate for the actual SS, i.e. least-squares linear regression slope and correlation coefficients ≈ 1 . Figure 1 shows the values of these statistics over a range of minimum liquid water content (LWC) and vertical wind velocity (w) cut-off values. We find that a LWC cutoff range $10^{-4} - 10^{-3.5}$ g/g yields the best results overall in this respect, regardless of w cutoff.
- Assuming the QSS approximation is valid as described above, the filter should have a minimal distorting effect on the form of the SS distribution. In particular, we want to avoid truncating the high-SS tail since these are of central importance in the consideration of the WPIM. In Figure 2 we show that, given the results from the previous point, a slightly less restrictive LWC cutoff is more appropriate in this second aim.

We therefore settled on the following criteria, which are used in all subsequent analyses:

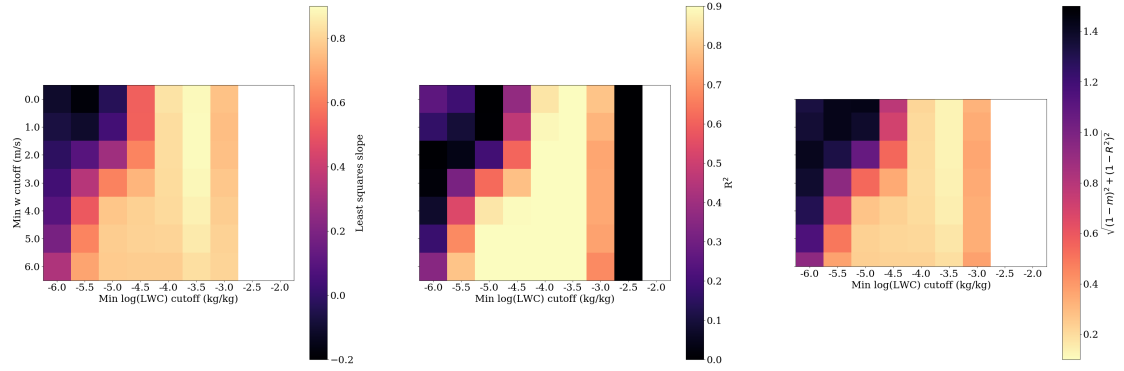
- $T > 273\text{K}$ (we're not including ice in the theory; note that Fan et al do evaluate SS wrt water above the freezing line though)
- $w > 2\text{ m/s}$ (reasonably strong updrafts) [*I realized when making the heatmaps that $w > 1$ gives just about the same level of agreement between SS_{QSS} and SS_{WRF} . Using this value instead would have the advantage of increasing the number of experimental data points that pass through the filter, without much change to qualitative or quantitative results. On the other hand, $w > 2$ is more consistent with what Fan et al do. I'm just going to leave this for now but it can easily be switched.*]
- cloud LWC $> 1\text{e-4 g/g}$ (in the convection core) [*I assume this 1e-4 LWC threshold is causing the sharp decrease in the number of qualifying points as you move up through 2 km. Can you reformulate this threshold to avoid the bias while retaining good agreement between SS and SS_{QSS} ? E.g., $\text{LWC} > 0.01 \times qv^*$? I realized I did not think through very carefully how I was graphing those distributions...the histograms in the righthand panels of Figure 4 show $\frac{dn_{\text{points}}}{dz}$, but the WRF grid is based on pressure coordinates, so this artificially skews the point number density low as you ascend in altitude. I've included a couple of figures at the end just graphing the absolute number of points vs z , which is less biased and also insensitive to the LWC cutoff (i.e. cutoff of 1e-4 vs 1e-5 kg/kg doesn't make a difference). Would it make sense to plot the histogram as $\frac{dn_{\text{points}}}{d \log z}$?*]

- including rain droplets and ventilation corrections

Figure 3 shows a scatterplot with the agreement between the actual and QSS-derived SS values in the WRF simulation, for points satisfying the above criteria. For brevity we will henceforth refer to such points as ‘cloudy updrafts.’

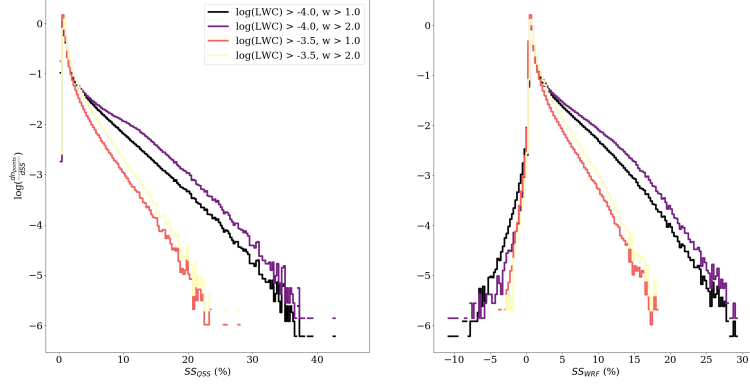


(a) Unpolluted case.

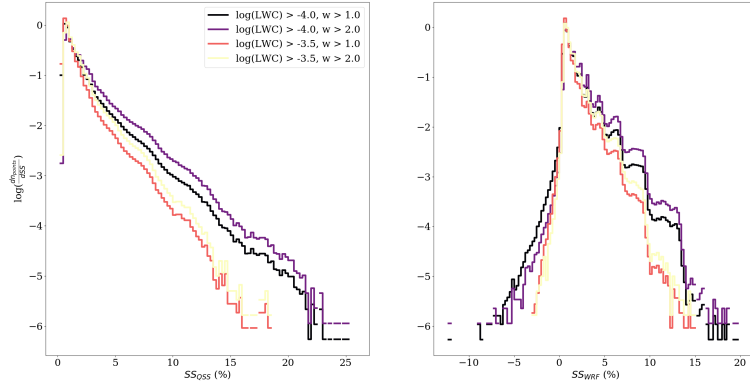


(b) Polluted case.

Figure 1: *[I have spent so much time trying to figure out how to correctly format the axes of this figure that I can no longer thing straight so I'm going to leave it and come back later...the two rightmost columns in each panel should be removed and the last panel should not be cut off at the top and bottom.]* Variation of (left) least-squares slope parameter and (center) correlation coefficient for SS_{QSS} vs SS_{WRF} with respect to cutoff values for LWC and w (in addition to imposing temperature cutoff, and inclusion of raindrops and ventilation corrections). Right panel shows Euclidean distance from the ideal point (1, 1) in the $m - R^2$ plane. *[Somewhat arbitrary but was looking for a way to visually combine the information in the left and center panels...]*

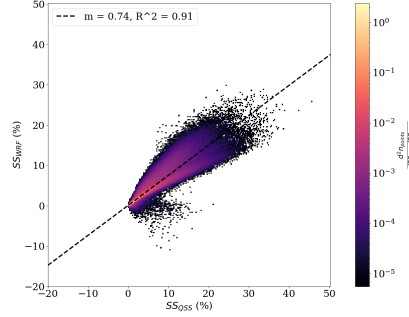


(a) Unpolluted case.

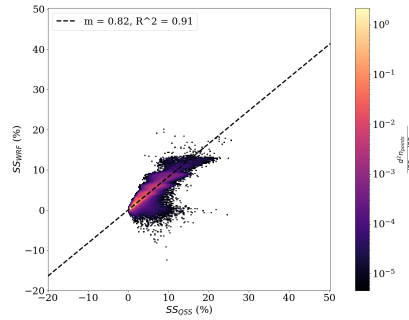


(b) Polluted case.

Figure 2: Normalized SS distributions after imposing filtering criteria on LWC and w (in addition to temperature cutoff, and inclusion of raindrops and ventilation corrections).



(a) Unpolluted case.




(b) Polluted case.

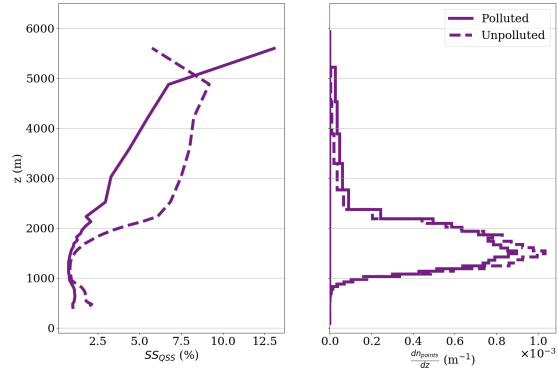
Figure 3: Actual (SS_{WRF}) vs predicted (SS_{QSS}) supersaturation. Color indicates density of data points; note the scale is logarithmic.

[*What were Fan's criteria?*] In their analysis, Fan et al use the following filtering criteria:

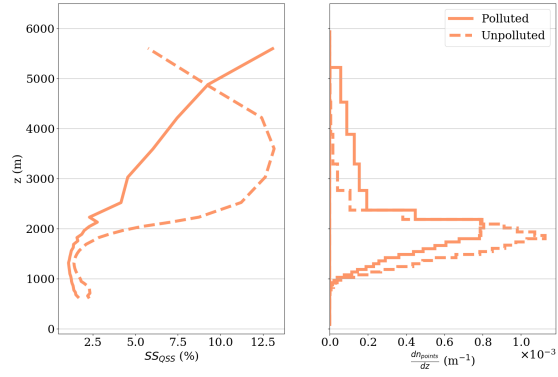
- For experimental data: They examine the upper 10th percentile of updrafts in “convective events” which 1) Fall between 11h00 and 19h00 local time 2) Have no other convective events occurring at any point in time 3 hours prior, and 3) Have max echo height at >0dBz above 10km. [*unfortunately there does not seem to be any definition of what actually qualifies as a convective event in the first place...*]. For aerosol measurements they take the average of measurements in the 30-min interval prior to the convective event.
- For model data: They limit analysis to a subset of the horizontal domain (red box in Fig S8) that encompasses a single convective event during the day of the simulation. They again take the top 10th percentile of updrafts with $w > 2$.



Because we use slightly different filtering criteria than that described above, we first verify that our selected cloudy updraft points yield similar SS profiles in the WRF simulation as those found in the latter work. In Figure 4 we plot vertical SS profiles for all cloudy updraft points, as well as for the upper 10 percentiles of all cloudy updraft points. We define the points in the “upper 10 percentiles” as those with w greater than the 90th-percentile (out of all altitudes and times) vertical wind velocity. *[Please define precisely. Upper 10th percentile of all grid points, or of all grid points at the same height? Within cloudy points? (The text here does not say anything about cloudiness, but the caption for Figure 2 does.) I have clarified how I am implementing this but neither the main text nor the SI of Fan’s paper provide any more precise language than “top 10 percentiles of updrafts”...Qindan I have been working under the assumption that this refers to w].* In [1] they consider a restricted subdomain around the T3 field station, indicated in Figure S8 of the supplementary information for that paper; we do not see a major qualitative difference when including this additional criterion; see Figure 16. We do indeed find the high SS values reported by Fan et al (maximum values of 13% in both polluted and unpolluted cases from the upper 10th percentile dataset), confirming that our filtering criteria establish a fair basis for comparison here. Note however that, in the righthand panels of Figure 4, the vast majority of cloudy updraft points are found at altitudes with relatively low average SS.



(a)



(b)

Figure 4: SS profiles (left) and number density of sampled points (right) for a) all cloudy updraft points; b) top 10% of cloudy updraft points with respect to vertical wind velocity, in WRF simulation conducted by Fan et al. Each point in the vertical profile represents an average over all times and horizontal coordinates for a given vertical grid coordinate.

We now seek to determine whether such high values actually occur in nature. First we look at data from the HALO flights in September and October of 2014 (see Methods/SI for details on selection of dates for this analysis) [*how to cite?*]. Figure 5 shows the analogue of Figure 4 using data from all HALO flight dates combined. We find no points with average SS above 1 %, even when limiting to the strongest updrafts in the combined dataset.

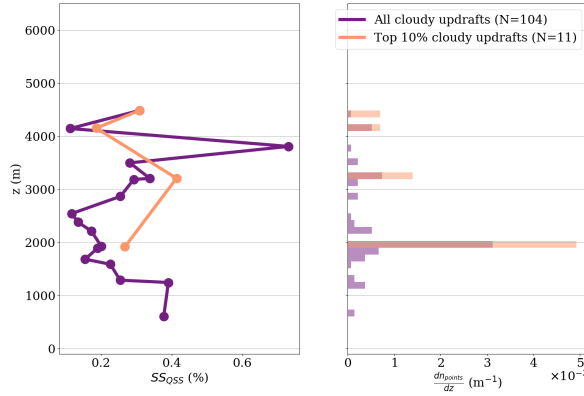


Figure 5: SS profiles (left) and number density of sampled points (right) from HALO flight campaign (all dates combined). Each point in the vertical profile represents an average over all times and horizontal coordinates for a given vertical interval (equally-spaced) [It does not look like the vertical intervals are equally spaced, nor would you want them to be, but I cannot tell what is actually going on. Why not pick a modest number N (e.g., 10) and group the samples by whether they fall in the quantile from 0 to $1/N$, from $1/N$ to $2/N$, etc. Then plot each of the N points in the left panel by the average of the height in that bin and the average SS in that bin. That is what I did here. $N=17$. Why do the top 10% w values occur at only four heights? Because I compare to 90th-percentile w out of all data points. Most altitude bins have less than ten points so it doesn't make sense to take upper 10 percentiles from each altitude bin. If n is the number density, then why are there more points at those heights in the upper 10% of w than there are with any w ? Because both of the distributions are normalized separately...if this is not conventional I can rescale]. SS profile is plotted with markers so as not to obscure intervals with missing data.

Finally, we examine a second experimental dataset from the first phase of the CAIPEEX campaign [13]. Although no $\text{UAP}_{<50}$ concentration measurements are available during this phase of the experiment, measurements of aerosols with diameters in the range of $0.1\text{--}3\text{ }\mu\text{m}$ showed total aerosol concentrations ranging from 700/ccm to 2500/ccm in the BL (see Figure 3(b) in [15] and Figure 4(a) in [13]). Reliable rain drop particle size distributions are unavailable from the flight dates in this analysis phase of the experiment, but we observe that exclusion of

raindrops from the calculation of QSS SS leads to a systematic overestimation of the true SS (see Methods/SI). Therefore we take the SS profiles in Figure 6 as an upper bound. We observe slightly higher values relative to those from the HALO flights, although we still don't find such high values as those output by the WRF models for the middle troposphere.

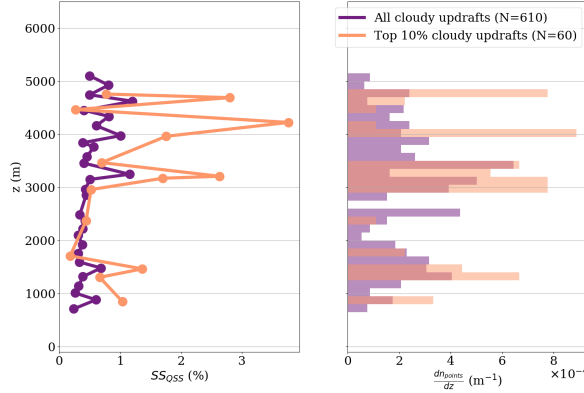


Figure 6: SS profiles (left) and number density of sampled points (right) from CAIPEEX flight campaign (all dates combined). Each point in the vertical profile represents an average over all times and horizontal coordinates for a given vertical interval (equally-spaced). SS profile is plotted with markers so as not to obscure intervals with missing data. See text for comments on the dataset.

We can use Equation 4 and the SS profiles in Figures 4-6 to infer a buoyancy profile for a hypothetical non-supersaturated parcel. For this analysis we take the temperature of the parcel equal to that of the environment (i.e., what has been measured). The resulting error in the value of δT in Equation 5 is quadratic in δRH , which is acceptable for our purposes. In Figure 7 we plot δT profiles from both WRF simulations and field campaigns side-by-side. We use these profiles to derive enhancements in $CAPE$ for the non-supersaturated parcel as:

$$\delta CAPE = g \int dz \frac{\delta T}{T} \quad (5)$$

where we again approximate T as the environmental temperature and integrate from 647 to 4488 m, the common vertical domain for all four curves in Figure 7. We find values of $\delta CAPE$ of 4, 6, 36, and 68 J/kg for HALO, CAIPEEX, WRF (polluted), and WRF (unpolluted), respectively. Neglecting any other physical energy sinks as above, these translate to vertical velocity enhancements of about 3 m/s in the field campaigns and 10 m/s in the simulations.

One possible counterargument is that the aerosol concentrations in the BL during the dates of the HALO flights might have been significantly higher

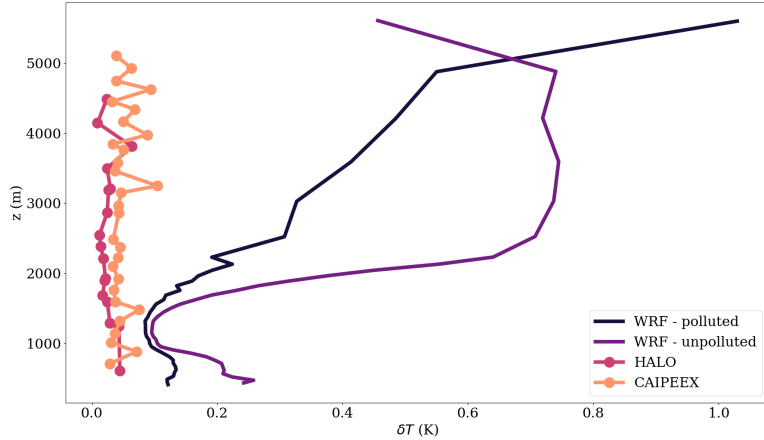


Figure 7: Profiles for δT of a non-supersaturated ($RH = 1$) parcel ascending in an environment with SS profiles shown in Figures 4-6, using Equation 5. SS profiles for HALO and CAIPEEX are plotted with markers so as not to obscure intervals with missing data.

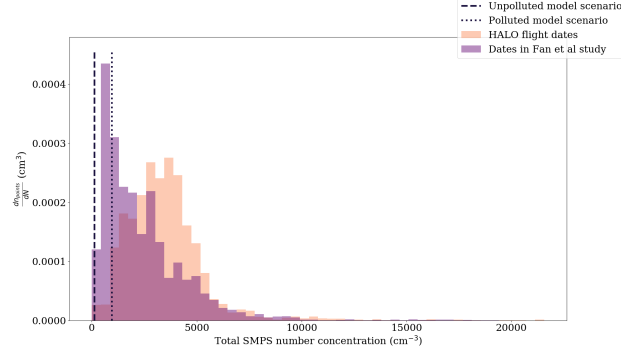
than those during the dates considered in Fan’s paper, thus precluding the occurrence of high SS values in the troposphere. In order to investigate this, we use the aerosol particle size distribution measured by the scanning mobility particle sizer (SMPS) in Manacapuru, located southwest of Manaus (PI: Chongai Kuang). This instrument measures particle concentrations in the diameter range 11.1-469.8nm. In Figure 8, we show that, while we do indeed see higher total aerosol concentrations on average during the HALO flight date range (3500/ccm vs 2400/ccm), the UAP50 concentration is on average lower (670/ccm vs 1600/ccm). In fact, the aerosol concentrations used in the WRF simulations are much lower than those observed during the day the simulation takes place, which is not justified quantitatively in that study.

We note additionally that the positive experimental correlation between concentration of UAP50 and maximum vertical velocity during the dates studied by Fan et al is not significant at the 95% confidence level - the least-squares slope parameter for their data set (the plot of which we reproduce in Figure 9, with additional 95% confidence bands) has a p-value of 0.11.

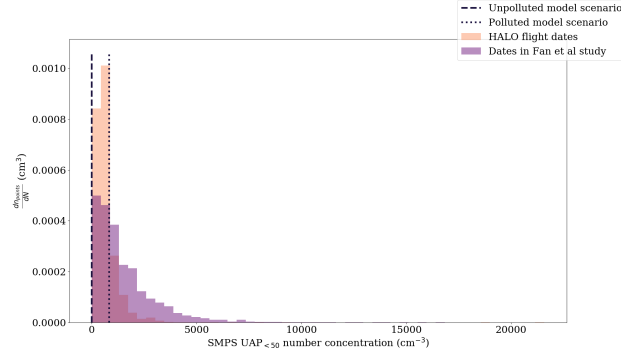
Another possible counterargument is that the flight campaigns simply didn’t fly through strong enough updrafts. However the vertical velocity distributions from the campaigns are quite similar to that from the simulations. See Figure 10.

Conclusion: The WPIM as proposed by Fan et al requires the average temperature profile of the troposphere to be set by relatively clean (high-SS) convection, in order for more polluted (low-SS) convection to experience an enhance-

ment in buoyancy. However, we find no evidence that the high SS values reported by Fan’s model actually occur in nature, which weakens the possibility of measureable invigoration effects - in particular, we estimate an upper bound on vertical velocity enhancement of ≈ 3 m/s from the HALO and CAIPEEX flight campaigns, compared to ≈ 10 m/s from Fan’s control simulations in WRF. The relatively low aerosol concentrations used to initialize the simulations, in combination with possible irregularities in microphysical parameterizations, may be to blame for the anomalously high SS values in the WRF output.



(a)



(b)

Figure 8: Distribution of aerosol concentration measurements by the ground-based SMPS at Manacapuru, Brazil; a) entire size range, b) only particles with diameter greater than 50nm. HALO flight dates are the same as those represented in Figure 5 (see Methods/SI for details). Dashed (dotted) lines show initial concentrations in the BL of the WRF simulation of polluted (unpolluted) conditions.

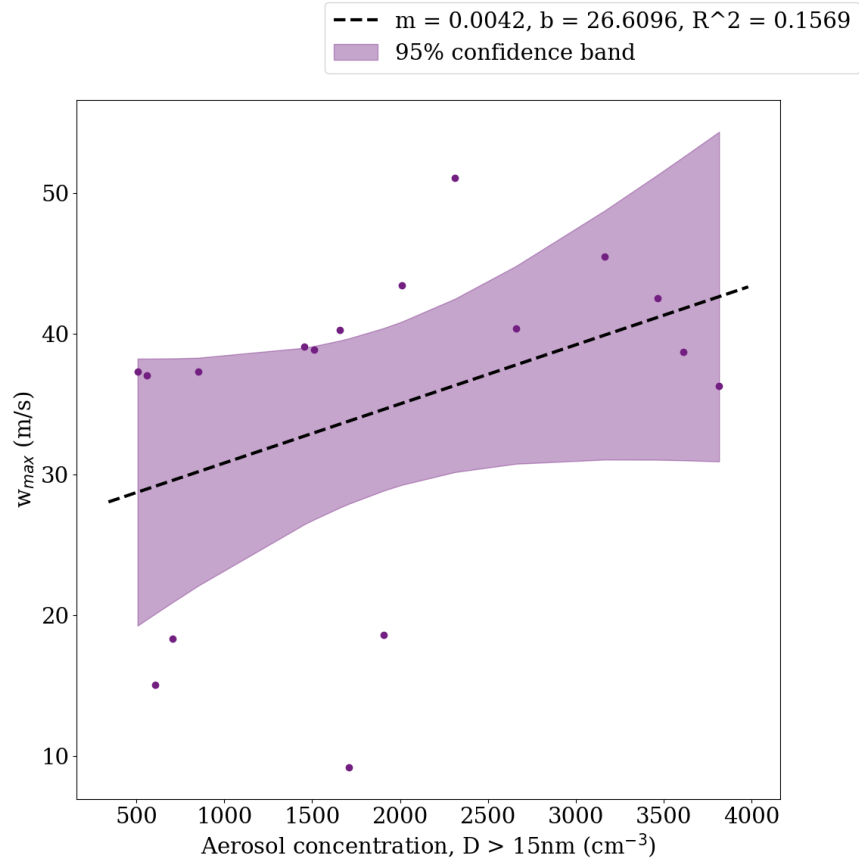


Figure 9: Ground-based total (including UAP50) aerosol concentration measurements versus maximum vertical wind velocity in convective cores; reproduced from Figure S2(a) of [1] with additional confidence bands our own.

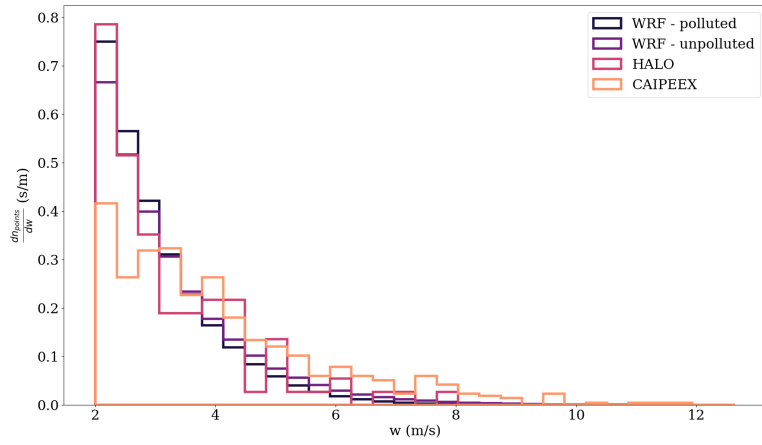


Figure 10: Vertical wind velocity distribution from simulations and field campaigns. Using filtering criteria outlined in the text.

3 Methods/SI

3.1 WRF

Model output for control simulations of polluted (“C_BG”) and unpolluted (“C_PI”) scenarios were provided by Fan et al; see that paper and accompanying SI for detailed explanations of model parameters and initializations.

In this paper, we use the following form of the QSS SS equation after [14] (with SS_{QSS} given as a percentage):

$$SS_{QSS} = \frac{A(T)w}{4\pi B(\rho_a, T)\langle f(r) \cdot r \rangle n} * 100, \quad (6)$$

where:

$$\begin{aligned} A(T) &= \frac{g}{R_a T} \left(\frac{L_v R_a}{C_{ap} R_v T} - 1 \right) (F_d(T) + F_k(T)) \\ F_d(T) &= \frac{\rho_w R_v T}{De_s(T)} \\ F_k(T) &= \left(\frac{L_v}{R_v T} - 1 \right) \frac{L_v \rho_w}{KT} \\ B(\rho_a, T) &= \rho_w \left(\frac{R_v T}{e_s(T)} + \frac{L_v^2}{R_v C_{ap} \rho_a T^2} \right) \end{aligned} \quad (7)$$

Notation for constants and variables is given in Table 1. We use the following parameterization for e_s [14]:

$$e_s(T) = 611.2 e^{\frac{17.67 T_c}{T_c + 243.5}}, \quad (8)$$

where T_c is the temperature in degrees Celsius.

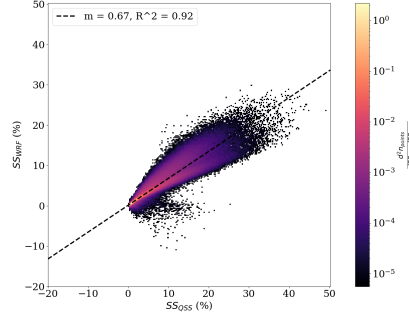
We note that this equation by also include finite size correction terms; however, using typical values for droplet salinity and condensation nucleus radius (the relevant parameters in this case), these terms are insignificant ($< 0.1\%$ correction to SS) for drops of radius greater than $3 \mu m$ [14], and we therefore do not consider them in this paper.

A simpler form of Equation 6 is often employed in the literature [2, 14], with:

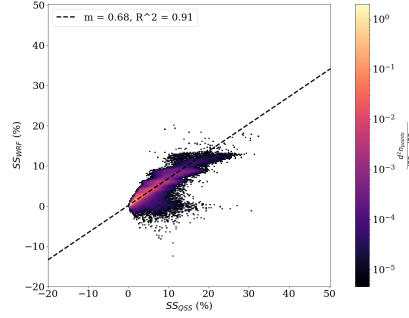
$$\begin{aligned} A(T) &= \frac{g}{R_a T} \left(\frac{L_v R_a}{C_{ap} R_v T} - 1 \right) \\ B(T) &= D \end{aligned} \quad (9)$$

Figure 11 shows that this form does not yield as good of agreement with the actual SS reported in WRF.

We use the expressions given in [16] and [14] for ventilation corrections [*They are kind of extensive...should I write out all formulae or just refer to the code in GitHub?*]. Figures 12 and 13 show, respectively, the effects of neglecting these corrections (i.e. setting $f(r) = 1$ for all r) for rain drops (defined here as



(a) Unpolluted case.



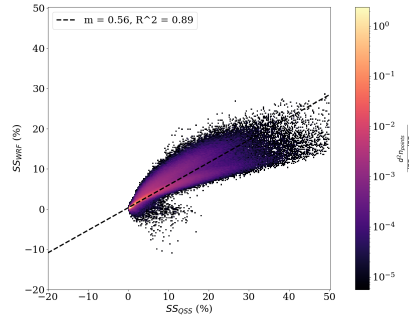
(b) Polluted case.

Figure 11: Actual (SS_{WRF}) vs predicted (SS_{QSS}) supersaturation, using simplified form of Equation 6. Color indicates density of data points; note the scale is logarithmic.

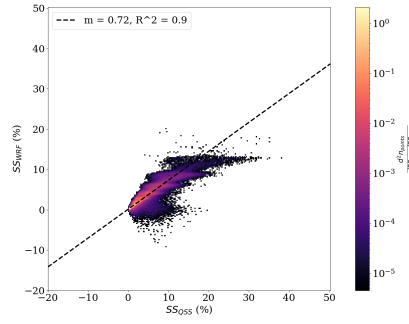
liquid water drops with diameter greater than $50 \mu\text{m}$), and omitting rain drops altogether from the calculations of mean radius and number concentration.

Finally, we note that we have excluded contributions to mean radius and number concentration from cloud droplets of diameter less than $5 \mu\text{m}$, for consistency with our analysis of HALO data (see proceeding subsection). In the end this yields values for SS_{QSS} which are indistinguishable to a reasonable number of significant figures.

Figures 14 and 15 show point distributions as absolute count rather than density with respect to z (since the WRF grid is spaced linearly in pressure rather than real-space coordinates). We see that the distribution is not very sensitive to LWC cutoff (which is lower by an order of magnitude in Figure 15).

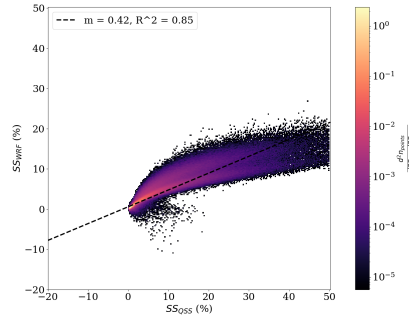


(a) Unpolluted case.

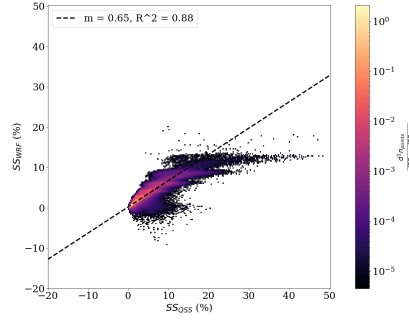


(b) Polluted case.

Figure 12: Actual (SS_{WRF}) vs predicted (SS_{QSS}) supersaturation, without ventilation corrections. Color indicates density of data points; note the scale is logarithmic.

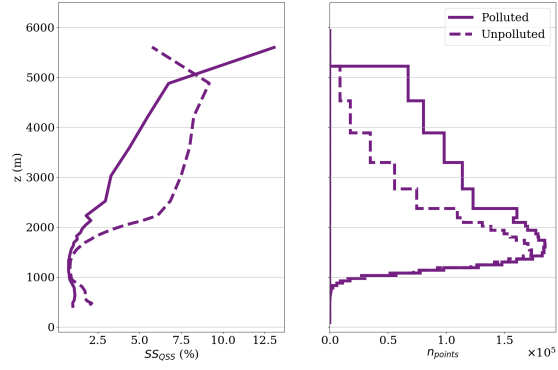


(a) Unpolluted case.

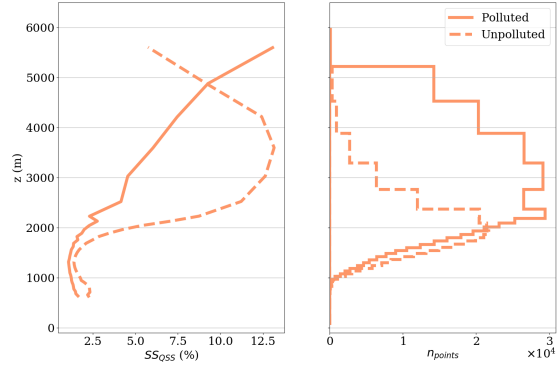


(b) Polluted case.

Figure 13: Actual (SS_{WRF}) vs predicted (SS_{QSS}) supersaturation, without contributions from rain drops. Color indicates density of data points; note the scale is logarithmic.

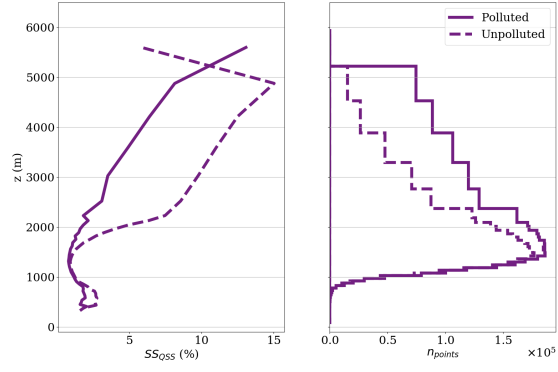


(a)

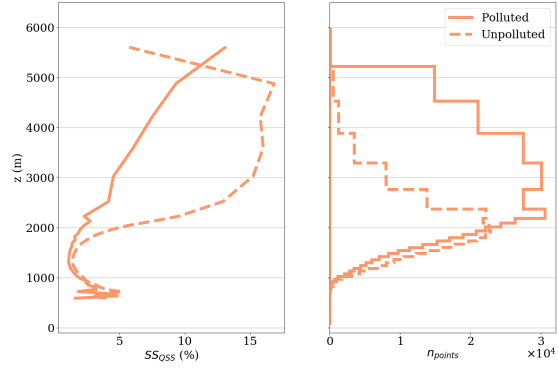


(b)

Figure 14: Identical to Figure 4 but righthand panel just shows absolute number of points per z -interval.



(a)



(b)

Figure 15: Identical to Figure ?? but with minimum LWC of $1.e-5$ rather than $1.e-4$ kg/kg.

3.2 HALO

The HALO aircraft supported two instruments for measuring cloud droplet spectra: a cloud and aerosol spectrometer (CAS-DPOL) and a cloud droplet probe (one element of a cloud combination probe) (CCP-CDP) [17]. We found that the CCP-CDP consistently reported unphysical bimodal size distributions, and therefore used only data from the CAS-DPOL for all calculations involving cloud droplets. Number concentrations from the CAS-DPOL were corrected using the ξ factor derived in [18].

The rain drop spectra came from data collected by greyscale cloud imaging probe (second element of the cloud combination probe) (CCP-CIP). The drop diameter detection ranges for CAS-DPOL and CCP-CIP were 0.89-50 μm and 25-2000 μm , respectively. Per guidance from the principal investigators for the CAS-DPOL, we only included data for droplets from size bins with a lower diameter bound greater than 3 μm in the analysis [19]. Effectively (given size bins for this instrument), this meant that the lower bound on diameter for water drops was 5 μm . Because the CAS-DPOL and CCP-CIP have overlapping diameter detection ranges, we use concentrations for particles between 5 and 25 μm from CAS-DPOL and from 25 to 2000 μm from CCP-CIP.

All measurements of environmental variables were taken from the Basic Halo Measurement and Sensor System (BAHAMAS).

Out of the dates for which all three instruments (BAHAMAS, CAS-DPOL, CCP-CIP) report data, we take those for which measurements of shared variables (true airspeed for BAHAMAS and CAS-DPOL; ξ correction factor for CAS-DPOL and CCP-CIP) are well-correlated (R^2 above 0.95). These are (all in 2014): 6, 9, 11, 12, 16, 18, 27, 28, 30 September; 1 October.

We used the same Equation 6 for SS_{QSS} and for ventilation factors as described above.

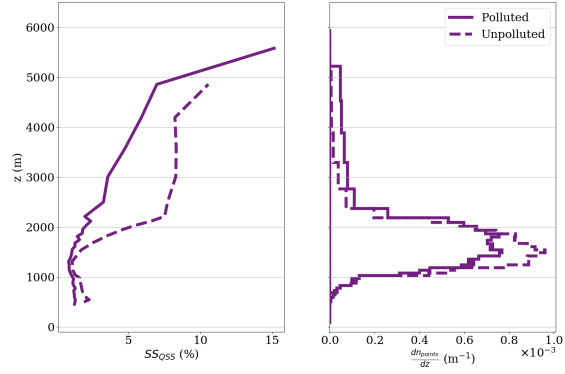
3.3 CAIPEEX

Cloud droplet spectra for phase 1 of the CAIPEEX field campaign were measured by a CDP (detection range 2-1562.5 μm). We used the data from the following flight dates in 2009: 16, 21, 22 June; and 18, 23, 24, 25 August.

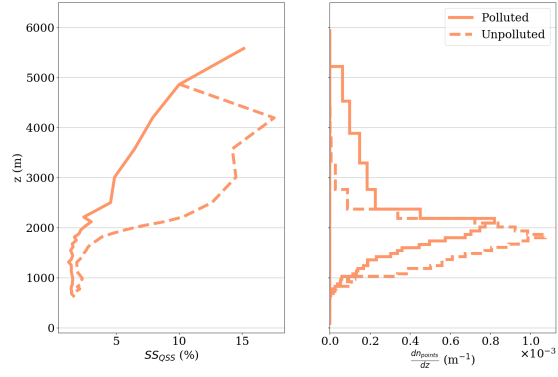
We used the same Equation 6 for SS_{QSS} and for ventilation factors as described above, and excluded data from cloud droplets of diameter less than 5 μm .

Symbol	Meaning	Value of constant	Notes
C_{ap}	Specific heat capacity at constant pressure, dry air	1005 J/kg	
D	Molecular diffusion constant of water in dry air	$0.23\text{e-}4 \text{ m}^2/\text{s}$	We take as constant wrt T
e_s	Saturation vapor pressure, water	-	
$f(r)$	Ventilation factor	-	
g	Gravitational acceleration on Earth	9.8 m/s	
K	Coefficient of thermal conductivity in dry air	$2.4\text{e-}2 \text{ J}/(\text{m s K})$	We take as constant wrt T
LWC	Liquid water content	-	
L_v	Latent heat of vaporization, water	$2.501\text{e}6 \text{ J/kg}$	We take as constant wrt T
N	Particle number concentration	-	
n_{points}	Point number density	-	Used for heatmap figures
q_v	Water vapor mass mixing ratio	-	Equals $\frac{m_w}{m_{tot}}$
q_v^*	Saturation water vapor mass mixing ratio	-	Equals $\frac{m_w^*}{m_{tot}}$
r	Particle radius	-	
RH	Relative humidity	-	Equals $SS + 1$
ρ_a	Mass density, dry air	-	Assuming ideal gas law
ρ_w	Mass density, liquid water	1000 kg/m ³	
R_a	Ideal gas constant, dry air	287.19 J/(kg K)	
R_v	Ideal gas constant, water	460.52 J/(kg K)	
SS	Supersaturation	-	Equals $RH - 1$
T	Temperature	-	
T_c	Temperature in degrees C	-	Equals $T - 273.15$
w	Vertical wind velocity	-	
z	Altitude	-	

Table 1: Explanation of constants and variables used in the paper.



(a)



(b)

Figure 16: Analogous to Figure 4 restricted to the horizontal subdomain indicated by the red box in Figure S8 (bottom left panel).

References

- [1] J. Fan, D. Rosenfeld, Y. Zhang, S. E. Giangrande, Z. Li, L. A. T. Machado, S. T. Martin, Y. Yang, J. Wang, P. Artaxo, H. M. J. Barbosa, R. C. Braga, J. M. Comstock, Z. Feng, W. Gao, H. B. Gomes, F. Mei, C. Pöhlker, M. L. Pöhlker, U. Pöschl, and R. A. F. de Souza, “Substantial convection and precipitation enhancements by ultrafine aerosol particles,” *Science*, vol. 359, pp. 411–418, 1 2018.
- [2] W. W. Grabowski and H. Morrison, “Do ultrafine cloud condensation nuclei invigorate deep convection?,” *Journal of the Atmospheric Sciences*, vol. 77, pp. 2567–2583, 7 2020.
- [3] W. W. Grabowski and D. Jarecka, “Modeling condensation in shallow non-precipitating convection,” *Journal of the Atmospheric Sciences*, vol. 72, pp. 4661–4679, 12 2015.
- [4] W. A. Hoppel, G. M. Frick, and J. W. Fitzgerald, “Deducing droplet concentration and supersaturation in marine boundary layer clouds from surface aerosol measurements,” *Journal of Geophysical Research: Atmospheres*, vol. 101, pp. 26553–26565, 11 1996.
- [5] F. Yang, R. McGraw, E. P. Luke, D. Zhang, P. Kollias, and A. M. Vogelmann, “A new approach to estimate supersaturation fluctuations in stratocumulus cloud using ground-based remote-sensing measurements,” *Atmospheric Measurement Techniques*, vol. 12, pp. 5817–5828, 11 2019.
- [6] M. Koike, N. Takegawa, N. Moteki, Y. Kondo, H. Nakamura, K. Kita, H. Matsui, N. Oshima, M. Kajino, and T. Y. Nakajima, “Measurements of regional-scale aerosol impacts on cloud microphysics over the east china sea: Possible influences of warm sea surface temperature over the kuroshio ocean current,” *Journal of Geophysical Research: Atmospheres*, vol. 117, pp. n/a–n/a, 9 2012.
- [7] M. K. Politovich and W. A. Cooper, “Variability of the supersaturation in cumulus clouds,” *Journal of the Atmospheric Sciences*, vol. 45, pp. 1651–1664, 6 1988.
- [8] N. Moteki, T. Mori, H. Matsui, and S. Ohata, “Observational constraint of in-cloud supersaturation for simulations of aerosol rainout in atmospheric models,” *npj Climate and Atmospheric Science*, vol. 2, 12 2019.
- [9] H. Siebert and R. A. Shaw, “Supersaturation fluctuations during the early stage of cumulus formation,” *Journal of the Atmospheric Sciences*, vol. 74, pp. 975–988, 4 2017.
- [10] C. Shen, C. Zhao, N. Ma, J. Tao, G. Zhao, Y. Yu, and Y. Kuang, “Method to estimate water vapor supersaturation in the ambient activation process using aerosol and droplet measurement data,” *Journal of Geophysical Research: Atmospheres*, vol. 123, 9 2018.

- [11] E. Hammer, N. Bukowiecki, M. Gysel, Z. Jurányi, C. R. Hoyle, R. Vogt, U. Baltensperger, and E. Weingartner, “Investigation of the effective peak supersaturation for liquid-phase clouds at the high-alpine site jungfraujoch, switzerland (3580 m a.s.l.),” *Atmospheric Chemistry and Physics*, vol. 14, pp. 1123–1139, 1 2014.
- [12] X.-Y. Li, G. Svensson, A. Brandenburg, and N. E. L. Haugen, “Cloud-droplet growth due to supersaturation fluctuations in stratiform clouds,” *Atmospheric Chemistry and Physics*, vol. 19, pp. 639–648, 1 2019.
- [13] J. R. Kulkarni, R. S. Maheskumar, S. B. Morwal, B. P. Kumari, M. Konwar, C. G. Deshpande, R. R. Joshi, R. V. Bhalwankar, G. Pandithurai, P. D. Safai, S. G. Narkhedkar, K. K. Dani, A. Nath, S. Nair, V. V. Sapre, P. V. Puranik, S. S. Kandalgaonkar, V. R. Mujumdar, R. M. Khaladkar, R. Vijayakumar, P. T. V., and G. B. N., “The cloud aerosol interaction and precipitation enhancement experiment (caipeex): overview and preliminary results,” *Current Science*, vol. 102, pp. 413–425, 2012.
- [14] R. R. Rogers and M. K. Yau, *A Short Course in Cloud Physics*. Butterworth Heinemann, 3 ed., 1989.
- [15] T. V. Prabha, A. Khain, R. S. Maheshkumar, G. Pandithurai, J. R. Kulkarni, M. Konwar, and B. N. Goswami, “Microphysics of premonsoon and monsoon clouds as seen from in situ measurements during the cloud aerosol interaction and precipitation enhancement experiment (caipeex),” *Journal of the Atmospheric Sciences*, vol. 68, pp. 1882–1901, 9 2011.
- [16] H. Pruppacher and J. Klett, *Microphysics of Clouds and Precipitation*. Springer Netherlands, 2010.
- [17] R. C. Braga, D. Rosenfeld, R. Weigel, T. Jurkat, M. O. Andreae, M. Wendisch, M. L. Pöhlker, T. Klimach, U. Pöschl, C. Pöhlker, C. Voigt, C. Mahnke, S. Borrmann, R. I. Albrecht, S. Molleker, D. A. Vila, L. A. T. Machado, and P. Artaxo, “Comparing parameterized versus measured microphysical properties of tropical convective cloud bases during the acridicon–chuva campaign,” *Atmospheric Chemistry and Physics*, vol. 17, pp. 7365–7386, 6 2017.
- [18] R. Weigel, P. Spichtinger, C. Mahnke, M. Klingebiel, A. Afchine, A. Petzold, M. Krämer, A. Costa, S. Molleker, P. Reutter, M. Szakáll, M. Port, L. Grulich, T. Jurkat, A. Minikin, and S. Borrmann, “Thermodynamic correction of particle concentrations measured by underwing probes on fast-flying aircraft,” *Atmospheric Measurement Techniques*, vol. 9, pp. 5135–5162, 10 2016.
- [19] T. Jurkat, R. Weigel, and C. Mahnke, “Private correspondence,” 2020.